ROYAL SOCIETY OF CHEMISTRY

PAPER

Check for updates

Structure, surface/interface chemistry and optical properties of W-incorporated β-Ga$_2$O$_3$ films made by pulsed laser deposition

Francelia Sanchez,[ab] Debabrata Das,[ac] Nathan Episcopo,[ac] Felicia S. Manciu,[d] Susheng Tan, [iD][e] Vaithiyalingam Shutthanandan [iD][f] and C. V. Ramana [iD] *[acg]

Gallium oxide (Ga$_2$O$_3$), which is one among the ultra-wide band gap materials, is promising for the next generation of electronic and optoelectronic devices due to its fascinating material properties for utilization in extreme environments. In this work, Ga$_2$O$_3$ films containing refractory tungsten (W) (GWO or Ga–W–O) were fabricated *via* pulsed laser deposition (PLD) by varying the oxygen partial pressure (pO$_2$), which is the most important thermodynamic parameter that governs the growth, structure and properties of the resulting multi-component oxide films. The effect of variable pO$_2$ on the structure, surface chemistry, chemical bonding, optical properties and photodetector device performance of the resulting Ga–W–O films was studied using X-ray photoelectron spectroscopy, Raman spectroscopy, atomic force microscopy, UV-vis spectroscopy, and photoluminescence spectroscopy measurements. The films containing Ga$_2$O$_3$ combined with W exhibited no secondary phase development. The impact of W on the chemical and optical characteristics of Ga$_2$O$_3$ films was found to be substantial. W^{5+} formation is prevalent when the adatom mobility is high at lower working pressure, whereas lower migration energy favors W^{6+} at higher working pressure. In contrast, the valance band maxima (VBM) of the films have a minor shift to higher energies with increasing pO$_2$, confirming the dominance of O 2p states on VBM in PLD GWO films. Additionally, there is not much change in the optical band gap, but it shows a slight blue shift of the luminescence peak, directing a selective W incorporation into the Ga$_2$O$_3$ matrix. The processing conditions were optimized to demonstrate the excellent performance UV-photodetectors based on PLD GWO films. The structure–property correlation established will be useful in the production of W-alloyed β-Ga$_2$O$_3$ films with superior structural and optical properties for integration into optoelectronic and photonic device applications.

1. Introduction

Among ultra-wide band gap (UWBG) oxide materials, gallium oxide (Ga$_2$O$_3$) is investigated as a promising candidate for the next generation of electronic and optoelectronic devices due

[a] *Center for Advanced Materials Research (CMR), University of Texas at El Paso, 500 W University Ave, El Paso, Texas 79968, USA. E-mail: rvchintalapalle@utep.edu*

[b] *Department of Metallurgical, Materials, and Biomaterials Engineering, University of Texas at El Paso, 500 W University Ave, El Paso, Texas 79968, USA*

[c] *Department of Aerospace and Mechanical Engineering, University of Texas at El Paso, 500 W University Ave, El Paso, Texas 79968, USA*

[d] *Department of Physics, University of Texas at El Paso, 500 W University Ave, El Paso, Texas 79968, USA*

[e] *Department of Electrical and Computer Engineering and Petersen Institute of Nano Science and Engineering, University of Pittsburgh, Pittsburgh, PA 15261, USA*

[f] *Environmental Molecular Sciences Laboratory, Pacific Northwest National Laboratory, 902 Battelle Blvd, Richland, Washington 99354, USA*

[g] *Physical and Computational Sciences Directorate (PCSD), Pacific Northwest National Laboratory (PNNL), Richland, WA 99352, USA*

to its desirable intrinsic material properties. Ga$_2$O$_3$ exhibits polymorphism and consists of six crystal structures: the rhombohedral α, monoclinic β, cubic γ, cubic δ, hexagonal ε, and orthorhombic κ phases.[1,2] Nevertheless, β-Ga$_2$O$_3$ received tremendous interest due to its chemical and thermal stability throughout all temperature ranges, from room temperature to its high melting point of ~1800 °C.[3] Further, high-quality β-Ga$_2$O$_3$ crystals that allow the growth of homoepitaxial films are readily available as they can be fabricated from the melt using the Czochralski, floating-zone, and edge-defined fed methods.[4] β-Ga$_2$O$_3$ is attractive due to its UWBG of ~4.9 eV and high theoretical breakdown field of 8 MV cm^{-1}. Some of the explored applications of β-Ga$_2$O$_3$ include high-power electronic devices, solar-blind photodetectors, light-emitting diodes (LEDs), chemical sensors, field-effect transistors (FETs), photocatalysis, *etc.*[3,5–9]

Historically, doping and alloying of semiconductors have been employed to tailor the structural, electrical, and optical properties.[10,11] N-type Si-doping is the preferred method to

control the electrical conductivity of β-Ga$_2$O$_3$ as the shallow donor successfully increases the concentration of free carriers by three orders of magnitude.[4,12] Further, because of their multiple states of charge, doping with transition metals (TMs) may promote more than one energy level.[13] Fe-dopant is a useful deep-level acceptor as it compensates background n-type carriers. Fe-doped β-Ga$_2$O$_3$ is commonly used as a semi-insulating crystalline substrate to grow homoepitaxial contact layers in β-Ga$_2$O$_3$ devices.[14,15] Semi-insulating substrates are desired to prevent conduction losses that causes degradation in device performance.[9] Moreover, doping with transition and rare earth elements (REs) into Ga$_2$O$_3$ has demonstrated interesting photoluminescence and electroluminescence properties.[7,8,11,15,16] Intentional doping with TMs and REs can facilitate light emissions in a broad spectral range, from ultraviolet (UV) to near-infrared (NIR). Solar-blind UV photodetectors were fabricated using Sn, Ta, and W dopants.[3,5,17] Cr-doped Ga$_2$O$_3$ exhibits strong NIR luminescence, which is desired to develop real-time optical imaging.[16] Further, monolithic, phosphor-free, multi-color LEDs was achieved from the pulsed laser deposition (PLD) of Ga$_2$O$_3$:(Tm + Eu + Er) multilayers on GaN and GaAs substrates as Eu, Er, and Tm doping intensify red, green, and blue electroluminescence emissions, respectively.[7,8] Undoubtedly, the tunable optical and electrical properties of Ga$_2$O$_3$ have potential for the design and development of next generation of electronic and optoelectronic devices.

In the present work, W-incorporated β-Ga$_2$O$_3$ thin films were fabricated by PLD. High-solubility of W ions into the β-Ga$_2$O$_3$ matrix and tuning of the electrical have been demonstrated elsewhere.[3,18–20] Our interest in the PLD W–Ga$_2$O$_3$ films is primarily towards the design and development of robust and advanced deep UV photodetectors for functionality in extreme conditions. Considering W-incorporation into Ga$_2$O$_3$ is due to the following fundamental scientific reasons. Tungsten is a refractory metal and has been considered as the potential contact layer for high-frequency electronic devices based on Ga$_2$O$_3$.[21,22] Additionally, tungsten oxide (W$_x$O$_y$) is also an attractive multifunctional material due to its intrinsic properties, including structural flexibility, the high melting temperature of approximately 1470 °C, and chromogenic behavior.[23–26] It has a wide range of applications in the energy sector, involving chromogenic devices to fabricate smart windows and photocatalysts to harvest solar energy.[24] W$_x$O$_y$ has been applied to gas sensors, water splitting, memory devices, and high-temperature diodes as a thin film.[23] Therefore, even if the processing conditions result in composite phase formation which occurs with individual component oxides in the matrix, excellent means to control the properties and performance is expected by taking the advantage of both Ga$_2$O$_3$ and WO$_3$. Moreover, the properties and performance of thin film-based devices strongly depend on the crystal quality of the films. Therefore, processing under optimum conditions of W-incorporated Ga$_2$O$_3$ expected to provide materials useful for electronic and optoelectronic device

applications. However, understanding the interplay between processing conditions, surface/interface microstructure, and optical properties is quite important in order to optimize the materials for enhanced performance in the device applications. In PLD, processing parameters such as temperature, atmospheric pressure, gas species, target material, and laser conditions influences the growth and structure of the resulting films and can be controlled to improve the properties and quality of the films.[3,11,27] Therefore, in this work, the effect of varying oxygen partial pressure (pO$_2$) on the optical properties, electronic structure, chemical composition, and morphology of the W-incorporated β-Ga$_2$O$_3$ films was investigated using multiple surface/interface characterization techniques in addition to probing material properties under variable growth conditions. We demonstrate that precise control over the deposition parameters allows tuning of the structure and optical properties of the Ga–W–O thin films for application in advanced, deep-UV photodetectors.

2. Experimental details

2.1. Materials and PLD target synthesis

Tungsten-incorporated β-Ga$_2$O$_3$ (hereafter, referred to GWO or Ga–W–O) PLD target was synthesized using the conventional solid-state reaction method. High-purity WO$_3$ (99.999%, Sigma Aldrich) and β-Ga$_2$O$_3$ (99.999%, Sigma Aldrich) powder precursors were weighed in stoichiometric proportions according to the chemical formula Ga$_{2-x}$W$_x$O$_3$ where x = 0.1. The powders were ground in an agate mortar under a volatile liquid environment (acetone) to decrease the particle size and ensure homogeneity. The homogeneous mixture was calcined in a SentroTech muffle furnace at 1100 °C for 12 h with a heating and cooling ramp rate of 5 °C min^{-1}.[3,18,28–31] The calcinated powder was mixed with polyvinyl alcohol (PVA) binder to create the target. The mixture was pressed using a uniaxial hydraulic press with an applied load of 1.5 tons for 3 min to shape the circular pellet with dimensions of 25.4 mm diameter and 5 mm thickness. The pellet was heated at 100 °C for 60 min to burn the binder material. After binder burnout, the pellet was sintered at 1350 °C for 12 h using a heating and cooling ramp rate of 5 °C min^{-1}.[3,18,28–31] The PLD target was examined thoroughly for structure, composition, and mechanical integrity to serve as a target for laser ablation before introducing it into PLD chamber for thin film deposition.

2.2. Pulsed laser deposition of GWO thin films

The GWO thin films were deposited onto Si(100) substrates by PLD. A KrF excimer laser with a wavelength of 248 nm and a pulse energy of 220 mJ was employed for the deposition process. The distance between the target and substrate was fixed at 45 mm. The substrate temperature and pulsed laser frequency were set at a constant value of 700 °C and 3 Hz, respectively. Note that, the substrate temperature (T_s) and oxygen partial pressure (pO$_2$) are the two most important

thermodynamic parameters that govern the film growth behavior and structure of the materials. While our previous work demonstrated that T_s = 700 °C is optimum to provide the sufficient thermal energy to promote the growth of crystalline films, in this work, pO_2 is varied in the range of 5–200 mTorr during deposition process.[3] The resulting films were subjected to extensive characterization in order to understand the effect of oxygen pressure on the surface/interface chemistry and optical properties of PLD grown GWO films.

2.3. Characterization

2.3.1. X-ray photoelectron spectroscopy (XPS). X-ray photoelectron spectroscopy (XPS) was used to measure the surface composition and chemical state of the elements in the W-incorporated β-Ga_2O_3 films. XPS measurements were performed using a Thermo Fisher Scientific Nexsa spectrometer consisting of a focused Al Kα monochromatic X-ray source (1486.6 eV) operated at 72 W and a high-resolution spherical mirror analyzer. The emitted photoelectrons were collected at the analyzer entrance slit located normal to the sample surface. The analyzer chamber pressure was maintained at ≈5 × 10^{-9} Torr. The survey spectra were recorded at a pass energy of 160 eV with a 0.5 eV step size, and high-resolution spectra were recorded at a pass energy of 50 eV with a step size of 0.1 eV. XPS data were analyzed by CasaXPS software.[32]

2.3.2. Raman spectroscopy. The Raman measurements were performed using an alpha 300RAS WITec confocal Raman system (WITec GmbH, Ulm, Germany), using the 532 nm excitation of a Nd:YAG laser and a 20× objective (Nikon, Japan). The system consists of a microscope coupled *via* an optical fiber of 50 μm core diameter with a triple grating monochromator/spectrograph and a thermoelectrically cooled Marconi CCD camera. Twenty spectra of 500 ms acquisition time each were co-added to improve the signal-to-noise-ratio. Spectral manipulations, such as baseline adjustment and normalization to the Si peak intensity, were also performed. The latter was to account for potential variations in the laser power output, which was kept at about 5 mW.

2.3.3. Transmission electron microscopy (TEM). FEI SCIOS FIB/SEM was utilized for the processing of TEM samples. The TEM imaging was conducted using the Thermo Scientific Titan Themis probe Cs corrected TEM, which was equipped with a SuperX EDS spectrometer. The instrument was operated at an energy of 200 keV. The use of High-angle annular dark-field scanning transmission electron microscopy (HAADF-STEM) was utilized to get insight into the structure and chemistry W-incorporated β-Ga_2O_3 thin films.

2.3.4. Atomic force microscopy. The surface morphology of the films was analyzed using atomic force microscopy (AFM; traxAFM) in constant force mode. The 1 × 1 μm AFM images were examined using the WSxM program to determine the estimated surface roughness.

2.3.5. Spectroscopic ellipsometry (SE). Spectroscopy ellipsometry (SE) measurements of the W-incorporated β-Ga_2O_3 films grown on Si substrate were analyzed using a Semilab SE-2000 instrument to investigate the optical constants (n and k) and thickness of the films. The values of Ψ (azimuth) and Δ (phase) were measured at room temperature in the standard acquisition mode over the wavelength range of 200–1650 nm, with a precision of 1 nm. The data was recorded at three angles of incidence (65°, 70°, 75°). The spectroscopic data was analyzed and modeled using Analyzer v1.6.6.2.

2.3.6. UV-vis optical (spectrophotometry) spectroscopy. Ultraviolet and visible (UV-vis) diffused reflectance spectroscopy was conducted using a JASCO V-770 spectrometer equipped with a single monochromator and an optical resolution of 0.3 nm to analyze the optical properties of the films. The diffuse reflectance spectra of the PLD GWO films deposited at variable pO_2 were measured. The reflectance spectra were converted to the Kubelka–Munk (K–M) function, which was utilized to determine the band gap of GWO films.

2.3.7. Photoluminescence (PL). The room-temperature photoluminescence measurements were determined using a Ti:sapphire laser with a wavelength of 245 nm and a frequency of 80 MHz. The samples were exposed to laser pulses with a duration of 100 fs and an incident power density of 5.5 kW cm^{-2}. A monochromator with a resolution of 0.02 nm and a photomultiplier tube were used to detect luminescence.

2.3.8. Device fabrication and characterization. Following a thorough analysis of the material properties, the most suitable sample was placed into a PVD chamber along with a metal shadow mask positioned at the front. A layer of silver (Ag), 100 nanometers in thickness, was applied on the surface. This was followed by a process of contact annealing that had been preoptimized. We employed a basic metal–semiconductor–metal (MSM) setup to do device characterization. The Keysight B1500A semiconductor device analyzer was used to measure the dark and photo I–V. The photoresponse of the manufactured MSM devices was investigated using 265 nm LED with different power output.

3. Results and discussion

3.1. Surface chemistry, electronic structure and chemical bonding

The elemental composition, chemical state, and electronic configuration were investigated using XPS. In Fig. 1(a), wide scan survey spectra confirm the presence of gallium (Ga), tungsten (W), and oxygen (O) XPS peaks. In addition, C 1s peak was identified due to carbon adsorption from exposure to air during the transfer of the samples to the XPS instrument. High-resolution XPS spectra of Ga 2p, O 1s, W 4f, and C 1s (not shown) were obtained to analyze each photoelectron region in greater detail. The binding energy (BE) scale of the scans was calibrated using a charge reference of the adventitious C–C/C–H peak to 284.8 eV.[33] The asymmetric O 1s peak, shown in Fig. 1(c), was
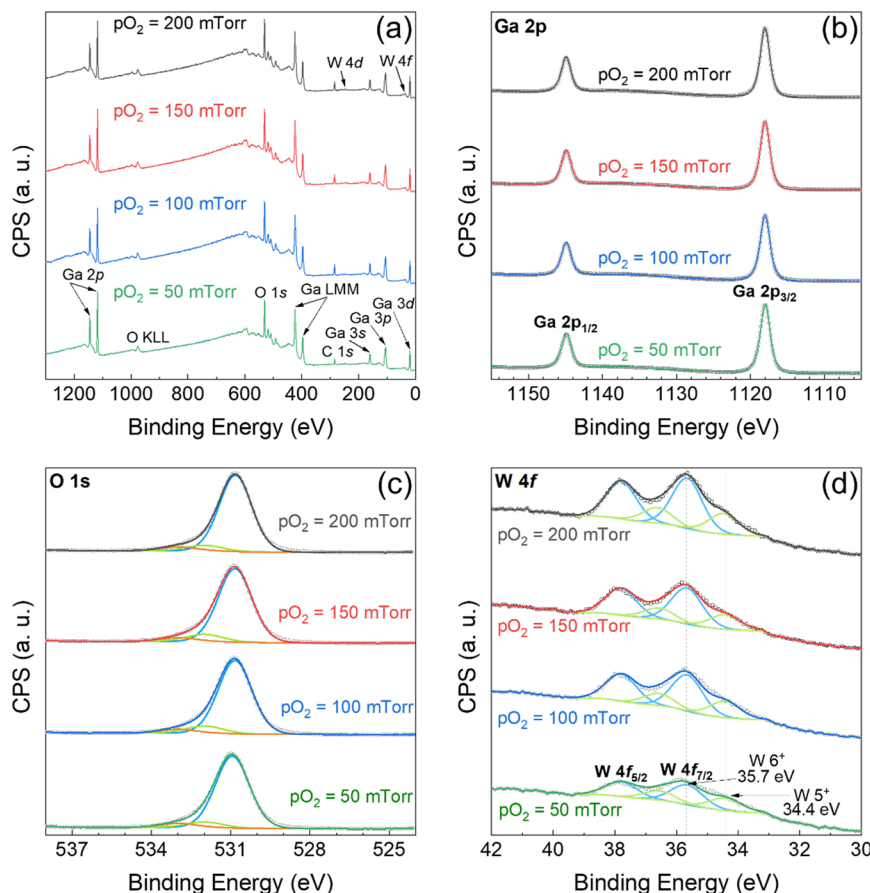
© 2024 The Author(s). Published by the Royal Society of Chemistry

RSC Appl. Interfaces, 2024, **1**, 1395–1409 | **1397**

Fig. 1 XPS data of the PLD W-incorporated β-Ga$_2$O$_3$ films deposited at varying pO$_2$. The data shown are: (a) survey XPS scan and high-resolution core level XPS spectra of (b) Ga 2p, (c) O 1s, and (d) W 4f. The data indicate a stable configuration of Ga ions irrespective of the pO$_2$ during deposition. The complex chemistry of W-ions depending on the pO$_2$ is evident from the data and analyses.

deconvoluted into three components after subtraction of a Shirley background. The main peak with high intensity is centered at 530.85 ± 0.05 eV, corresponding to the metal oxide lattice bonds between Ga and O or W and O. The shoulder peaks at higher binding energies demonstrate partial surface contamination caused by sample handling. The peaks positioned at 532 and 533 eV are assigned to the covalent bonds between carbon and O in the organic hydroxyl (C–O) and carbonyl (C=O) groups, respectively.[18,28,34]

The high-resolution Ga 2p core level spectra are illustrated in Fig. 1(b). The data shown are for GWO samples deposited at different pO$_2$. For further analyses and to probe changes in chemical stoichiometry as a function of pO$_2$ and W-incorporation, the Ga 2p core level was preferred over Ga 3d because of its high intensity and isolated position, avoiding interference or overlapping with other electron peaks. The peaks identified correspond to the doublet Ga 2p$_{3/2}$ and Ga 2p$_{1/2}$. The former peak positioned at a BE ∼ 1118.1 ± 0.1 eV is attributed to the Ga^{3+} ions of stoichiometric Ga$_2$O$_3$.[18,28–30] The doublet peaks have a spin–orbit splitting (ΔE = BE Ga 2p$_{3/2}$ − BE Ga 2p$_{1/2}$) of 26.9 eV. As shown in Fig. 1(b), there is no appreciable change in the shape and position of the Ga peaks. Therefore, the chemical valence state of Ga ions is very

stable throughout the PLD deposited W-incorporated β-Ga$_2$O$_3$ samples despite the W incorporation and the varying pO$_2$ during deposition.

Detailed core level spectra of the W 4f are depicted in Fig. 1(d). The analysis of the W 4f spectra is difficult because of its changing background, the possible presence of multiple chemical states, and the proximity to the W 5p$_{3/2}$ region.[35,36] The iterative Shirley method was used to correct the complex background with step changes.[35] The doublet, namely W 4f$_{7/2}$ and W f$_{5/2}$, is visibly identified on the spectra. Distinctly, peaks are asymmetric due to the co-existence of more than one valence state of W within the surface of the PLD GWO films. The binding energies of W^0, W^{4+}, W^{5+}, and W^{6+} in the W 4f$_{7/2}$ region are reported to be at 31.4, 32.9, 34.6, and 35.9 ± 0.2 eV, respectively.[36] The W 4f spectra were deconvoluted into two components using a mixed Gaussian–Lorentzian (GL30) line shape. The higher binding energy peak is centered at 35.7 eV, corresponding to the highest valence state of W, W^{6+}. The shoulder peak on the right is positioned at a lower binding energy of 34.4 eV and is assigned to reduced W^{5+} ions. In fact, the W$_x$O$_y$ chemistry is very complex because of its structural flexibility and cation intermediate states.[24,36] The W–O system contains numerous

oxides with variable chemical valence states, namely, WO_3, $WO_{2.9}$, W_3O_8, W_5O_{14}, $W_{18}O_{49}$, and $W_{24}O_{68}$, among others.[24,25] The reduced oxides commonly occur as the lattice can sustain high O vacancies and partially reduced W^{5+} species. The electronic density near the W valence states increases with O vacancies since the electronegativity of O is greater than W.[37,38] Therefore, the electron binding energy of W^{5+} is in lower energy levels because of the high concentration of electrons surrounding it. Furthermore, the W 4f peaks show a gradual increase in peak intensity as a function of pO_2. Evidently, the W content increases with increasing pO_2. In addition, the peaks in Ga 2p and W 4f have minimal narrowing with the increasing pressure. Decay in full width at half maximum (FWHM) may be caused by improvement in the crystallinity of the films.[39]

The chemical and electronic structures of the films are highly dependent on their growing conditions.[40] In depositing complex multicomponent target material such as β-$Ga_{2-x}W_xO_3$, the discrete plasma plume species travel at different velocities because of their dissimilar ionic mass and size.[41] Background gas pressure can control the number of collisions between gas and plasma plume species. Consequently, background pressure tailors the kinetic energy of the species arriving on the substrate. The mean free path (MFP) is the ratio between the distance traveled and the number of collisions between species, which is approximated using the equation:

$$\lambda = \frac{k_B T}{\sqrt{2} P \pi d_m^2} \tag{1}$$

where k_B is Boltzmann's constant, T is temperature, P is pressure, and d_m is the mean diameter of the gas and species. Due to their different ionic size, the mean free path differs between species, and they arrive at the substrate at different times. At a given pressure, smaller particles have a larger mean free path and higher kinetic energy. Background gas pressure is categorized into three regimes: vacuum-like low pressure, transition regime, and diffusion-like regime.[41,42] In the vacuum-like regime, there are minimal interactions between the background gas and the plasma plume species. Due to their high migration energy, some of the plasma species might rebound from the substrate. In this regime, O vacancies can easily form. In addition, lower crystallinity and roughness are expected from the low interaction between species before arrival to the substrate. Within the "transition" pressure scheme, the number of collisions between background gas and plasma plume increases. This regime facilitates the incorporation of O species in the film as the formation energy of O vacancies increases with pO_2. Therefore, the probability of O defects decreases with higher pressures. As a result, the structural quality of the film increases. In the diffusion-like pressure conditions, the MFP is smaller than one-tenth of the target-to-substrate distance. At these high background gas pressures, there is a high number of interactions between plasma plume species and background gas that reduce the

energy of the species rapidly. Further, cluster formation is favorable due to the great interaction between species. The plasma plume might be forced to rebound to the ablated target at even higher pressures due to a transient high local pressure created by a trapped portion of the background gas near the substrate holder. At these high pressures, crystal quality is expected to decrease.

Furthermore, the changes in stoichiometry and electronic structure, such as W content and valence states, are attributed to the varying pressure. Though the ionic size between Ga and W is similar, W content at the surface varies with gas pressure. Fig. 2(a) depicts the ratio of $W^{5+}:W^{6+}$ ions as a function of pO_2. W is deficient at the lower pO_2, whereas its incorporation improves as the pressure increases. First, there is a greater amount of Ga ions in the plasma plume because of the Ga-rich target composition. For this reason, the Ga content is high and very stable in all the samples, as demonstrated by XPS analysis. Moreover, the lower content of W ions is slightly smaller than that of Ga ions.[43,44] Thus, at a given pressure, W species have greater migration energy than Ga. In vacuum-like pressure, the W ions travel with high kinetic energy and are more likely to outdiffuse from the surface of the substrate.[3] With the increasing pressure, the migration energy of the W species decreases as a result of greater interaction between O and the plasma plume species. These collisions promote nuclei and cluster formation. Consequently, W incorporation is improved in the films. This pressure regime is known as diffusion-like growth. However, the presence of W^{5+} is accompanied by O defects on the surface. Clearly, the amount of W^{5+} species decreases with the increasing pressure. The formation of W^{5+} indicates non-stoichiometric growth of reduced W^{6+} due to O deficiency.[37,38,45–49] Note that the ionic ratio is drastically higher when the film is deposited at a pO_2 of 50 mTorr in comparison with higher pO_2. O-vacancies can easily form in vacuum-like low pressures due to insufficient interaction between background gas and plasma plume species. Nevertheless, the formation energy of O vacancies increases with higher pO_2.[50,51] The incorporation of O species in the film is improved by increasing collisions between gas and plasma plume species. As a result, the structural quality of the film increases. Overall, W^{5+} formation is prevalent when the adatom mobility is high, and it is observed with higher temperature, lower working pressure, or lower laser power density. In contrast, lower migration energy favors W^{6+}.[38,46–49,52–55] Additionally, the crystal structure of the samples improves as the concentration of O defects decreases with the higher background pressures. Conclusively, the formation of W^{5+} reduced ions, increasing W content, and improving crystalline structure are a result of the dissimilar mean free path of the species with varying pO_2. Thus, the XPS studies indicate that a pO_2 of 100 mTorr or higher will be needed in order to realize GWO films without any compositional defects, particularly those related to reduced states of W-ions. Such defects may introduce additional localized states in the electronic structure and can shift the
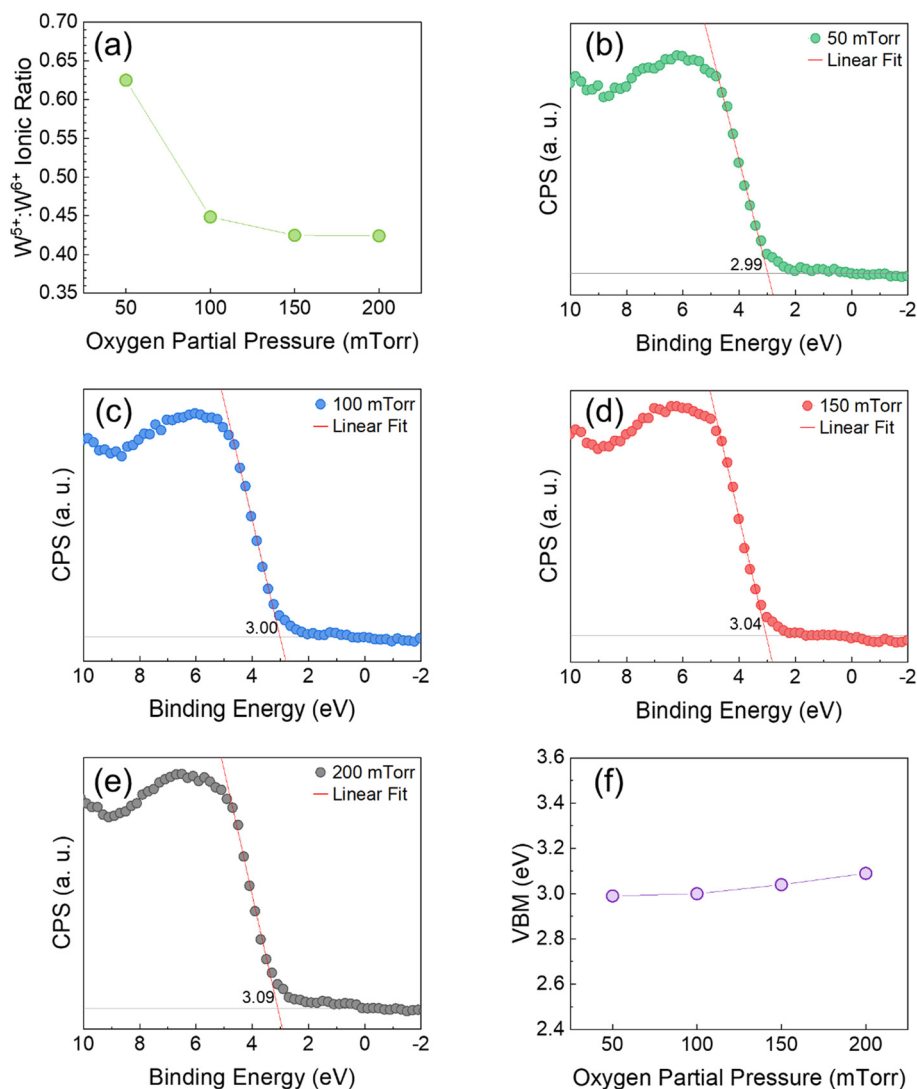
© 2024 The Author(s). Published by the Royal Society of Chemistry

RSC Appl. Interfaces, 2024, **1**, 1395–1409 | **1399**

Fig. 2 (a) Surface $W^{5+}:W^{6+}$ ionic ratio of the W-incorporated β-Ga_2O_3 films as a function of pO_2. (b–e) Extrapolated valence band XPS spectra of the films and (f) variation in valence band maxima with increasing pO_2.

band gap dramatically. This scenario will result in the performance degradation of UV-photodetector based on GWO films.

Having understood the chemistry of GWO films using core-level XPS, we now direct our attention to the density of electronic states. The high-resolution valence band XPS spectra demonstrate the density of electronic states in the lowest BE region. In addition, it can provide the valence band maxima and the Fermi-level position relative to VBM.[28] In Fig. 2(b–e), the valence band maxima (VBM) of the samples were determined from the linear extrapolation of the leading edge to the background line at zero counts in the valence band spectra. The Fermi-level position with respect to the surface VBM is defined by the BE corresponding to 0 eV. The linear extrapolation of the leading edge in the valence band spectra of Ga_2O_3 is simple and has been used in multiple XPS analyses of different materials. The VBM of films may vary due to processing conditions, microstructure, elemental

composition, defects, etc.[28,34,56–60] The VBM of the samples as a function of pO_2 is depicted in Fig. 2(f). As seen, the VBM of the films has a minor shift to higher energies with increasing pO_2. It is believed that the changes in VBM are associated with the varying W content rather than lattice defects, as there are no significant changes in the position and shape of Ga 2p peaks in Fig. 1(b). The minimum increase in VBM with the increasing W concentration is expected as O 2p states dominate the VBM.[57–59]

The Raman spectra of GWO grown at different pO_2 pressures are shown in Fig. 3a. For comparison, the spectrum of bulk monoclinic β-Ga_2O_3 is also presented in Fig. 3b. The latter is shown for easier observation of potential changes of β-Ga_2O_3 vibrational lines with W incorporation. There is no visible difference between the spectra of GWO due to pO_2 pressure growth. While in the low- and mid-frequency regions (120–550 cm^{-1}), the strong Si peak at 521 cm^{-1} and the unwanted but conspicuous presence of Si–O bonds at 303 cm^{-1}
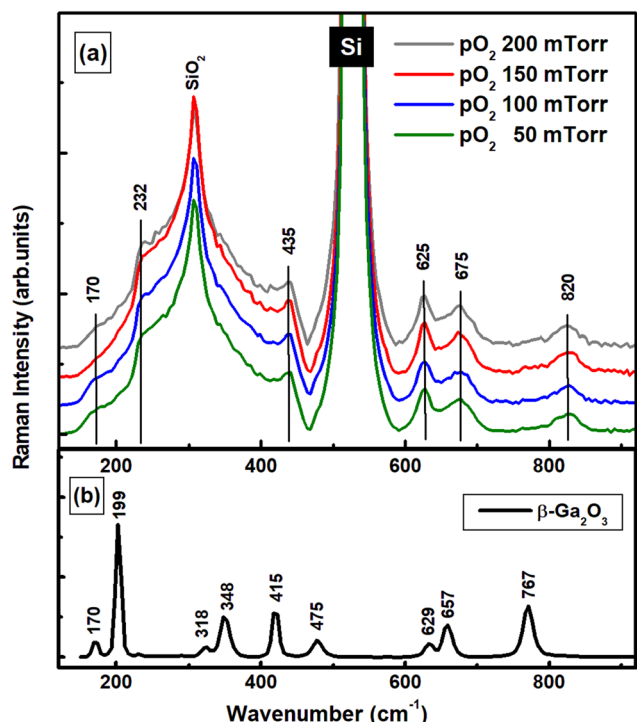
Fig. 3 (a) Raman spectra of W-incorporated β-Ga$_2$O$_3$ films deposited under variable pO$_2$. (b) Raman spectrum of bulk β-Ga$_2$O$_3$.

dominate the spectra of GWO. However, the two weak shoulders at 170 cm^{-1} and 232 cm^{-1} could infer the presence of β-Ga$_2$O$_3$.[61] The latter is blue-shifted by 33 cm^{-1} from the characteristic vibrational line at 199 cm^{-1} (Ag). Similarly, the weak feature at 435 cm^{-1} can be attributed to a shifted β-Ga$_2$O$_3$ vibration at 415 cm^{-1} (Ag). It can also be associated with SiO$_2$ presence. Shifts in phonon frequencies due to size confinement effects are expected and have been reported in low-

dimensional materials.[62] Additionally, the vibrational modes can experience positive or negative shift when the dopant into host matrix is different in terms of atomic mass despite the solid solubility.[63] The small thickness of the GWO film, in addition to contributing to the weakness of vibrational lines associated with the material of interest, cannot mask the strong presence of Si and SiO$_2$ seen. Other peaks in the high-frequency region (500–770 cm^{-1}) associated with O–Ga–O stretching and bending modes of GaO$_4$ units of β-Ga$_2$O$_3$ are observed at 625 and 675 cm^{-1} in the GWO spectrum. They are attributed to the red and blue shifted lines at 629 and 657 cm^{-1} of β-Ga$_2$O$_3$, respectively. The disappearance of the 767 cm^{-1} vibration of β-Ga$_2$O$_3$ and the appearance of the weak and broad band at 820 cm^{-1} in the GWO spectrum is potentially correlated with the incorporation of W into the gallium oxide structure by substitution of W-ions at the Ga-ions sides and formation of vacancies.

3.2. Morphology and microstructure

The surface morphology of PLD deposited GWO films was analyzed using the AFM measurements. The 2D topographical scans of the W-incorporated β-Ga$_2$O$_3$ films are shown in Fig. 4(a–e). In addition, the root-mean-square surface roughness was calculated to quantify the effect of pO$_2$ on the surface morphology of the PLD GWO films. There is an evidence for the granular morphology of the PLD GWO films, where that the nanoscale grain structure increases in size with increasing pO$_2$. This observation is commonly observed in many of the simple and complex metal-oxide films made by PLD, specifically for samples grown under increasing pO$_2$.[64–66] In fact, at least for the specific case of PLD oxide films, increasing pO$_2$ induces the grain-growth under the reactive atmosphere, which in turn roughens the samples' surface leading to changes in the optical properties.[65] On the other
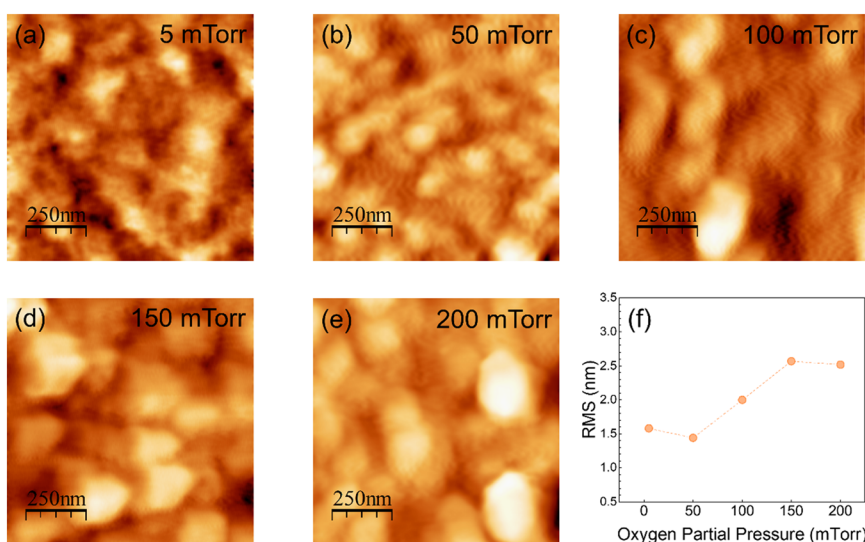

Fig. 4 AFM data of PLD GWO films deposited at varying pO$_2$. (a–e) AFM surface morphology scans; and (f) RMS roughness variation with pO$_2$ for PLD GWO films. The effect of pO$_2$ on the morphology and roughness of PLD GWO films is evident.

© 2024 The Author(s). Published by the Royal Society of Chemistry

RSC Appl. Interfaces, 2024, **1**, 1395–1409 | **1401**

hand, comparable to XPS data revealing the chemical composition and complex chemistry of W-ions under variable pO_2, the AFM results are highly susceptible to the growth kinetics of the films. In Fig. 4(a), the scanned image of the film deposited at a low pO_2 of 5 mTorr reveals a non-uniform surface. As discussed earlier, due to the minimal interaction between gas and plasma plume species, poor crystallinity, low roughness, and high concentration of surface defects, such as O vacancies, are expected in films grown at vacuum-like pressures. With the increasing pressure, at 50 mTorr, the surface is somewhat uniform, and the grain structure is well defined. Furthermore, the roughness slightly decreases, which might be due to the fulfillment of O-vacancies. As the pO_2 increases, the film grows in a diffusion-like regime, where the roughness increases due to the larger crystals formed from the undergoing cluster growth. Even at a higher pressure of 200 mTorr, the roughness is relatively non-affected by the higher pO_2. Overall, an increased O gas pressure leads to the formation of denser and more uniform films with larger grain sizes. Additionally, surface features have a great effect on the optical properties of films.[34,48] On the other hand, PLD GWO film thickness is varying from ~50 to ~200 nm with pO_2 but we believe the effect of the AFM on surfaces is a true reflection of the effect of pO_2 instead of thickness since we made extensive studies previously on pure Ga_2O_3 films with variable thickness. Thus, the XPS and AFM studies indicate that the stoichiometric GWO film growth with good surface morphology can be obtained for pO_2 of 100 mTorr and higher.

After understanding the surface chemistry and morphology of the PLD GWO films, we directed our efforts to understand their microstructure and surface/interface chemical composition profiles using high-resolution transmission electron microscopy (HRTEM) studies. Fig. 5 depicts the high-resolution cross-sectional morphology and elemental color mapping of a representative PLD GWO film ($pO_2 = 100$ mTorr) on Si substrate. Cross-sectional HAADF-STEM image (Fig. 5a) clearly shows the presence of sharp transition from the substrate to the W-incorporated β-Ga_2O_3 film at the interface. There is no evidence of Ga assisted reverse etching of the substrate during the first nucleation phase at the start of the growth process. Additionally, the elemental color mapping and the atomic percentage plots (Fig. 5b and c) confirm the presence of evenly distributed O, Ga, and W atoms. Also, their relative percentages match the stoichiometry, highest for O and lowest for W.

Finally, before proceeding to evaluate the optical properties of PLD GWO films, we present a brief summary of crystal structure analyses made by X-ray diffraction (XRD) studies. The effect of pO_2 on the crystal structure and phase stabilization of GWO films has been reported elsewhere in detail.[3] In XRD, all the peaks observed were in excellent agreement with β-phase Ga_2O_3 and no diffraction peaks due to WO_3 were observed. However, somewhat broader and asymmetric peaks related to β-Ga_2O_3 were noted. When these results combined with aforementioned Raman spectroscopic data, it appears that heavier W ions substituting for relatively lighter Ga ions may cause some lattice strain. On the other hand, the difference in
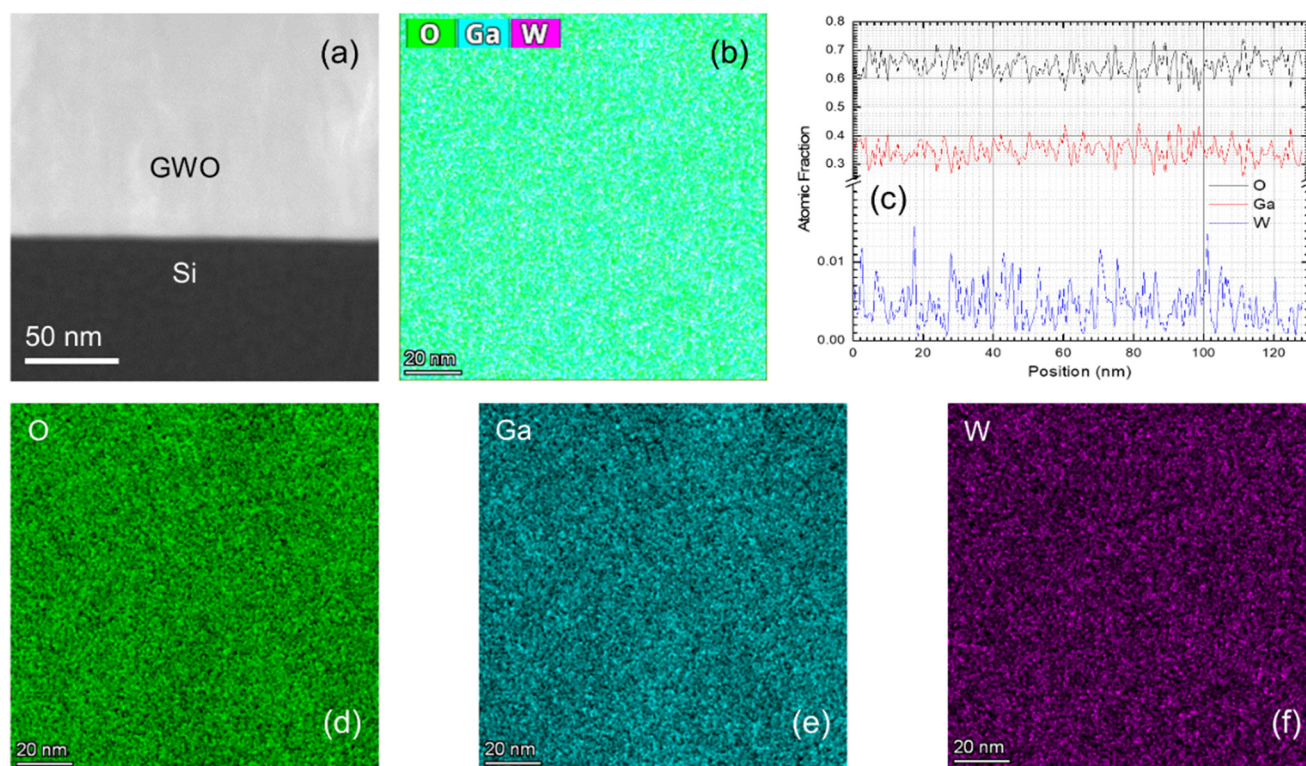

Fig. 5 Cross sectional TEM images: (a) high-resolution HAADF STEM images of W-incorporated β-Ga_2O_3 films on a Si platform. (b and c) Elemental color mapping and corresponding atomic fraction plots for Ga, O, and W, respectively. (d–f) Individual color mapping of O, Ga, and W.

the ionic radii of Ga^{3+} and W^{6+} is relatively small (the ionic radius of Ga^{3+} and W^{6+} is 0.062 and 0.060 nm, respectively) suggesting the solid solution should be possible provided the temperature and oxygen pressure are optimum. Indeed, the XRD studies indicated that the PLD GWO films were crystallized in β-phase Ga_2O_3.[3] However, GWO films deposited at relatively lower pO_2 (5–50 mTorr) are of not high quality while those deposited at higher pO_2 were textured and stabilize in β-Ga_2O_3 films. The crystal quality improves with increasing pO_2 for the PLD GWO films. Therefore, summarizing intermittently based on the structure, surface chemistry, chemical bonding, and surface morphology studies of PLD GWO films deposited at variable pO_2, oxygen pressure of 100 mTorr or higher results in the stoichiometric, crystalline GWO films with β-phase and good surface quality as desired for UV-photodetector applications.

3.3. Optical properties

3.3.1. Spectroscopic ellipsometry. The optical properties and the growth behavior of the W-incorporated β-Ga_2O_3 films were probed by spectroscopic ellipsometry (SE). SE measures the polarization changes upon the interaction of light with matter. The experimental values, Δ and Ψ, denote the phase shift and amplitude ratio, respectively, of the perpendicularly polarized waves reflected from the surface of the sample.[67] Changes in polarization are defined by the following equation:

$$\rho = \frac{R_p}{R_s} = \tan \Psi e^{(i\Delta)} \qquad (2)$$

where R_p and R_s are the complex reflection coefficients of the light polarized parallel and perpendicular to the plane of incidence, respectively.[67] The experimental and calculated values of Δ and Ψ measured at different angles are depicted in Fig. 6(a and b). The model spectra were calculated using a Tauc–Lorentzian (TL) dispersion model and a Gaussian oscillator. The TL model is commonly applied in the analysis of transparent and semi-transparent semiconductors, and it is defined by the following equation:
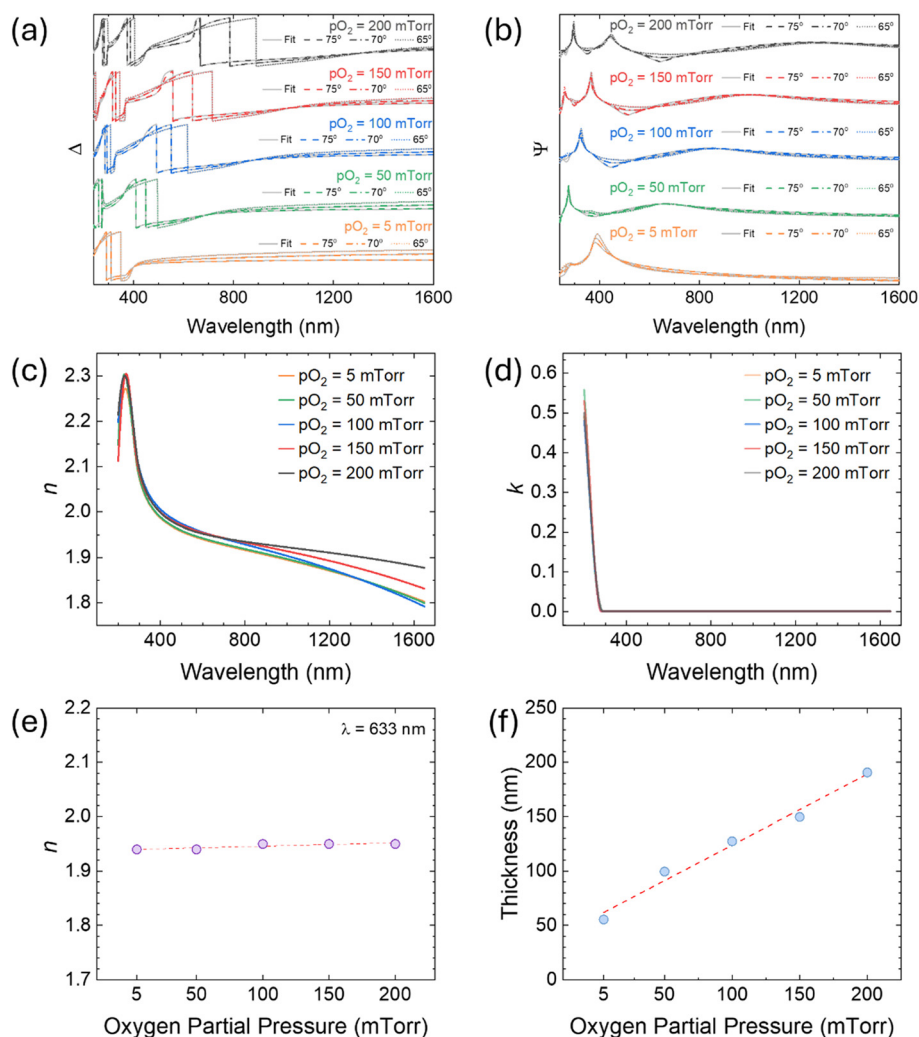

Fig. 6 SE data of as-grown samples. (a and b) Representative plots of psi and delta functions extracted at different angles of incidence of the sample grown at varying pO_2. (c and d) Refractive index and extinction coefficient of all the samples. (e and f) Refractive index at a wavelength of 633 nm and pressure-dependent thickness variation of all the samples.

© 2024 The Author(s). Published by the Royal Society of Chemistry

RSC Appl. Interfaces, 2024, **1**, 1395–1409 | **1403**

$$\varepsilon_{2TL}(E) = \frac{AE_0C(E-E_g)^2}{(E^2-E_0^2)^2+C^2E^2}\frac{1}{E}, \ E > E_g; \ \varepsilon_2(E) = 0, \ E \leq E_g \quad (3)$$

whereas the Gaussian model is often used to describe the optical function spectra of crystalline phases and is denoted by the equation:

$$\varepsilon_{2G_{osc}}(E) = \frac{A}{C}e^{-\left(\frac{E-E_0}{C}\right)^2} + \frac{A}{C}e^{-\left(\frac{E+E_0}{C}\right)^2} \quad (4)$$

where A is the amplitude, C is the oscillator width, E_0 resonant energy, and E_g is the optical band gap energy.[68–70] The TL oscillator models the spectra near the bandgap energy, whereas the Gaussian model is useful to fit the spectra below the bandgap.[71] The real parts of the dielectric functions are calculated using the Kramers–Kronig (KK) relation.[68] The refractive index (n) and extinction coefficient (k) as a function of wavelength are shown in Fig. 6(c and d). There are no observed changes in the extinction coefficient of the films. There is a slight increase of refractive index with the increasing pO_2. Film thickness measured by ellipsometry is portrayed in Fig. 6(f). Clearly, the thickness increases with pO_2 as there are more interactions between O_2 and plasma species that decrease their kinetic energy and facilitate film growth.

3.4. UV-vis spectroscopy

UV-vis diffuse reflectance spectrum of the W-incorporated β-Ga_2O_3 films on a silicon substrate was obtained to derive the bandgap of the films. Since the band gap energy

transition (E_g) is not as notorious in the diffuse reflectance spectra, the reflectance spectra were converted to the Kubelka–Munk (K–M) function, which is directly proportional to the absorption coefficient as follows:

$$F(R) = \frac{(1-R)^2}{2R} = \frac{K}{S} \quad (5)$$

where R is the reflectance, and K and S are the absorption and scattering coefficients, respectively.[72] Consequently, $F(R)$ can substitute the absorption coefficient in the Tauc equation:

$$(\alpha h\nu)^n = A(h\nu - E_g) \quad (6)$$

where α is the absorption coefficient, $h\nu$ is the energy of the incident photon, A is the proportional constant, and n is a unitless parameter with a value of 2 for direct transition and $\frac{1}{2}$ for indirect transition. The direct optical band gap energy was calculated by linear extrapolation of the Tauc plot using the Kubelka–Munk (K–M) method versus photon energy since $E_g = h\nu$ when $(F(R)h\nu)^n = 0$ as shown in Fig. 7(d and e). The E_g variation as a function of pO_2 is presented in Fig. 7(f). The bandgap energy of the films oscillates between 4.7 and 4.9 eV and is in good agreement with the reported values in the literature.[11,27,28,73] The optical bandgap increases with increasing pO_2 between 5 to 150 mTorr. Crystalline structure, chemical composition, surface morphology, and defects influence the reflectance spectra and energy bandgap.[6,34] Due to its minimal content and variation, W incorporation might not affect the bandgap tailoring. However, in correlation with
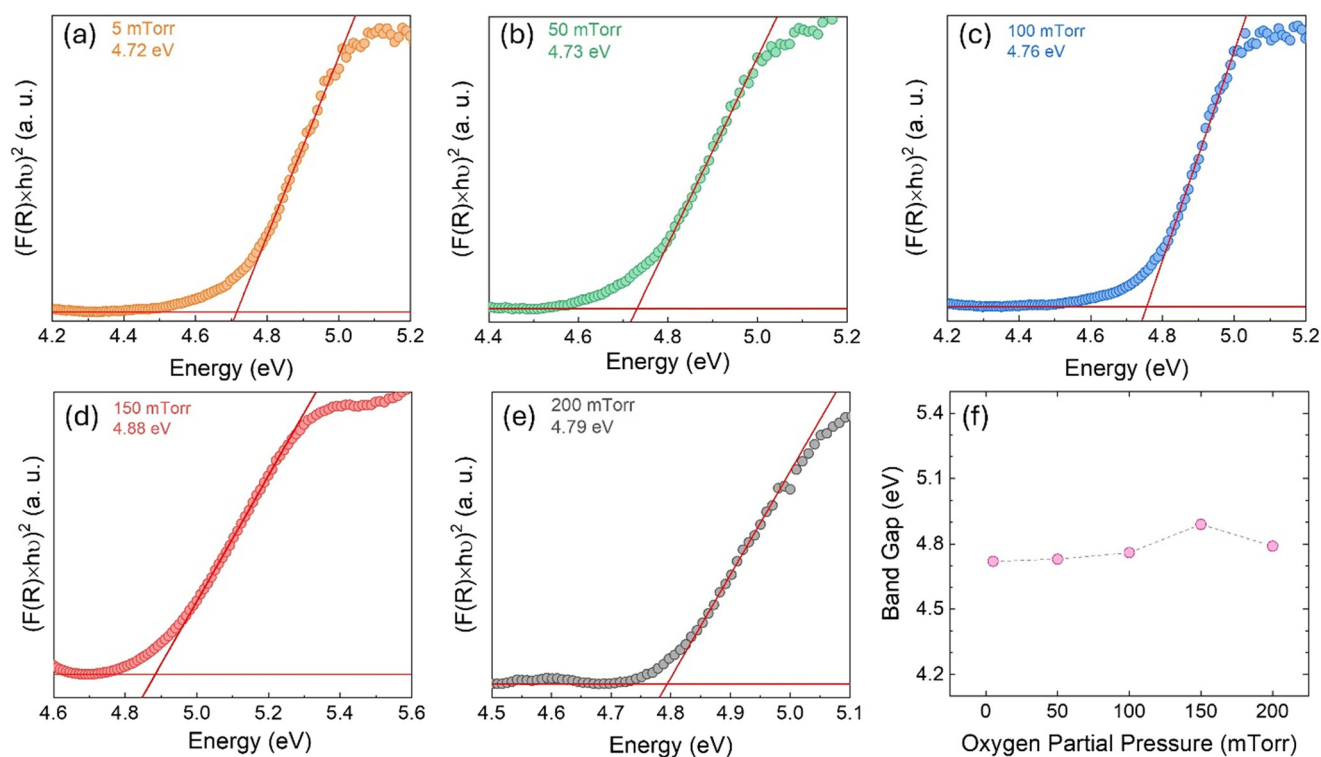

Fig. 7 (a–e) Tauc plots originated from UV-vis reflectance spectra for bandgap calculation using linear extrapolation. (f) Bandgap energy variation as a function of pO_2.

© 2024 The Author(s). Published by the Royal Society of Chemistry

the previous results, pO_2 strongly influences the structure and properties of the films. In fact, O vacancies can be responsible for the bandgap narrowing of the films grown at lower pO_2. The defect states of O vacancies can form before and overlap with the valence band edge, thus reducing the bandgap.[6,34] Nevertheless, band gap energy increases as a function of pO_2 as the formation energy of O vacancies increases in an O-rich environment. Further, at the higher pO_2 of 200 mTorr, a lower band gap energy is observed and can be associated with the higher W content in the films.[19]

3.5. Photoluminescence spectroscopy

Photoluminescence (PL) measurements were obtained to further understand the electronic structure and defect states of the W-incorporated β-Ga$_2$O$_3$ films with varying pO_2. PL spectroscopy is very useful in characterizing semiconductor materials because it reveals the recombination dynamics of photo-generated carriers and detects optically active intrinsic and extrinsic defect states.[3,74] The room temperature steady-state PL spectra of the W-incorporated β-Ga$_2$O$_3$ films are illustrated in Fig. 8. The PL data was collected in the wavelength range of 250 to 800 nm. The PL spectra of each sample exhibit an asymmetric peak due to the presence of multiple luminescence bands. The luminescence behavior of β-Ga$_2$O$_3$ is well-established in the literature. The peak position and peak intensity of the PL transitions depend on the trap-state density of the films that were manipulated by adjusting the deposition conditions, such as substrate

temperature and working pressure. In the W-incorporated β-Ga$_2$O$_3$ films, three PL bands corresponding to blue, green, and red emissions are observed. The blue and green emissions are reported to originate from recombining the donor–acceptor pair (DAP). In the blue band, the Ga–O pair and Ga vacancies (V_{Ga}) act as the acceptor, and O vacancies (V_O) correspond to the donor, and in the green emissions, the V_O and Ga_i serve as donors.[75,76] Clearly, there is a gradual red shift of the peaks with increasing deposition pressure. As observed in XPS results, the W content in the films increases with pressure. Thus, the gradual red shift of the peaks is associated with the incorporation of W.

Substitutional W in β-Ga$_2$O$_3$ is a potential triple donor since W at Ga sites can provide a maximum of three extra electrons.[77] W atoms in β-Ga$_2$O$_3$ may occupy tetrahedral or octahedral sites. The inequivalent Ga sites in the unit cell of β-Ga$_2$O$_3$ are depicted in Fig. 9(a). Octahedrally coordinated W serves as a deep donor and has a lower formation energy than W on tetrahedral sites, which acts as a shallow donor. The formation energy of W on octahedral sites is lower because of the lower Fermi-level position of the charge-state transition levels and smaller local distortion in the lattice.[77] Therefore, there is a preferential formation of substitutional W on octahedral positions that serve as deep donors and introduce the red PL emission. The empirical valence and conduction band diagram calculated from the XPS, UV-vis, and PL spectra analysis of the W-incorporated β-Ga$_2$O$_3$ films grown under different pO_2 are shown in Fig. 9(b). The slight changes in the density of states diagram are associated with
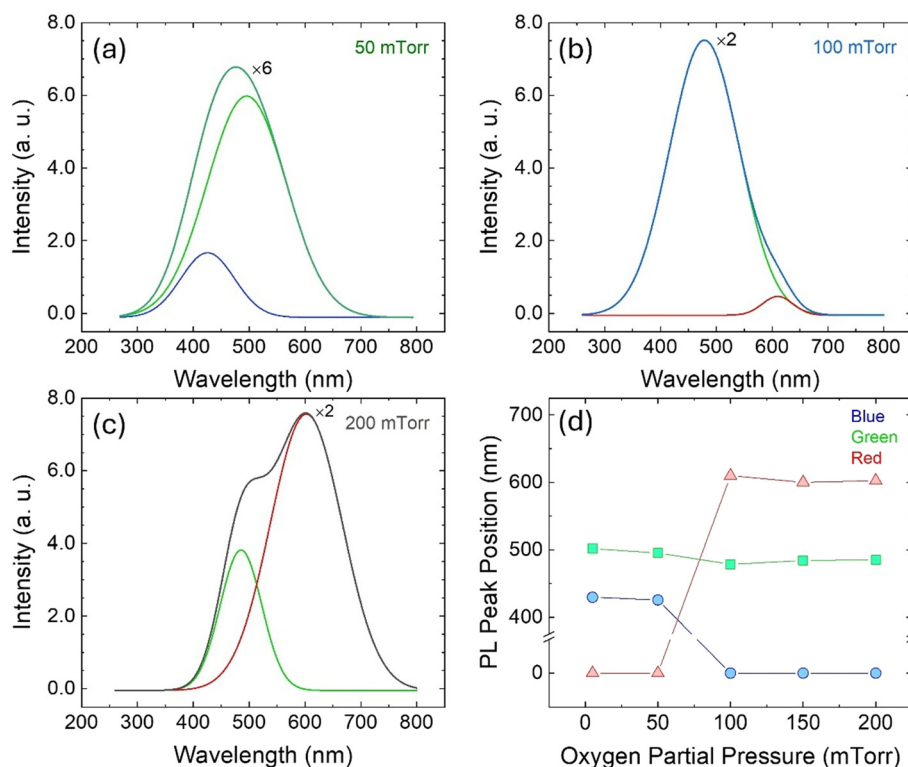

Fig. 8 (a–c) Room temperature PL spectroscopy of the W-incorporated β-Ga$_2$O$_3$ films. (d) PL peak position as a function of pO_2.
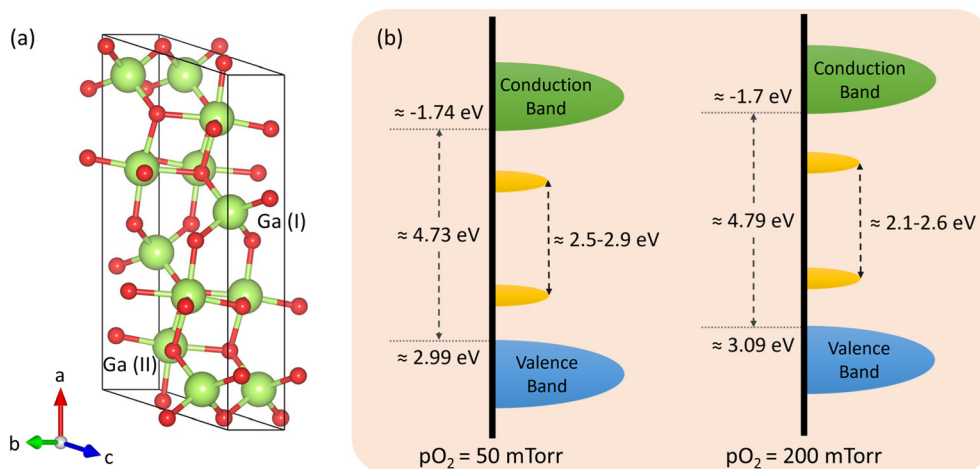
Fig. 9 (a) Crystal structure of the monoclinic β-Ga₂O₃. The inequivalent Ga(ɪ) and Ga(ɪɪ) sites refer to the tetrahedral and octahedral positions, respectively. (b) The schematic density of states diagram, calculated from XPS, UV-vis, and PL spectroscopy, of the W-incorporated β-Ga₂O₃ films grown under O₂-poor and O₂-rich conditions.

the varying elemental composition and concentration of defect states. The increase in the VBM in O₂-rich environment is caused by the higher W content, whereas the band gap narrowing in O₂-poor conditions is due to the high concentration of O vacancies.

By establishing a correlation between chemical, optical, and luminescence properties, it can be inferred that the development of W-incorporated β-Ga₂O₃ thin films with tunable emission bandwidth is significantly influenced by the pO₂. By employing meticulously regulated *in situ* variables, it becomes feasible to exhibit superior stoichiometric W-incorporated β-Ga₂O₃ on external substrates, enabling its subsequent use as effective visible-emitting phosphors in smart LED applications. In tandem with the development of contemporary civilization and technological progress, the global community is moving towards effectively utilizing current energy sources. To address this issue, a crucial measure is to eradicate ineffective artificial light sources and substitute them with intelligent, energy-efficient phosphor-converted light-emitting diodes (pc-LEDs). The current state of pc-LEDs mainly depends on rare earth (RE) minerals as either bulk or dopants, which poses challenges in terms of energy efficiency due to their toxicity and limited availability.[7,8] The W-incorporated β-Ga₂O₃ thin films stated above can be a strong alternative to RE-based phosphors and can be easily integrated with current semiconductor nanofabrication methods for pc-LEDs.

3.6. Deep-UV photodetection

We have constructed a basic metal–semiconductor–metal (1 × 1 mm MSM) ultraviolet photodetector (PD), in which W-doped β-Ga₂O₃ is used as the active material and a silver top metal contact is employed. Since the fundamental material characterization using a wide variety of surface analytical techniques indicated that the samples deposited at

lower pO₂ were containing various defects and pO₂ ∼ 100 mTorr was optimum to produce GWO films with better quality, the photodetector sandwich structures were made on PLD GWO films made at 100 mTorr. The simple manufacturing procedure and low-cost metal contact were chosen to show a cost-effective UV solar-blind photodetection method. Significantly, the Ag and W-doped β-Ga₂O₃ are establishing a Schottky contact, as seen in Fig. 10. The metal–semiconductor interface's carrier exchange process is mostly controlled by thermionic emission, which needs a lot of energy to get past the normal Schottky junction limit. Moreover, there exists a specific likelihood of thermionic field emission or field emission-assisted tunneling occurring throughout the depletion zone. The metal–semiconductor interface trap states are crucial to tunneling.

We used 265 nm photoexcitation and gradually increased the illumination power density. The existence of a metal–semiconductor Schottky junction in a back-to-back configuration is responsible for the nonlinearity seen in the current–voltage (J–V) characteristics of the 100 mTorr sample, as shown in Fig. 10a. We set a constant bias of 10 V and computed the responsivity (R), detectivity (D^*), external quantum efficiency (EQE), and photo-to-dark current ratio (PDCR) while gradually varying the illumination power density to better understand the photodetector's performance. Common photodetector (PD) parameters R, D^*, EQE, and PDCR can be stated as follows.

$$R_\lambda = \frac{j_{p,\lambda} - j_d}{P_\lambda} \tag{7}$$

$$D^* = \frac{R_\lambda}{(2ej_d)^{1/2}} \tag{8}$$

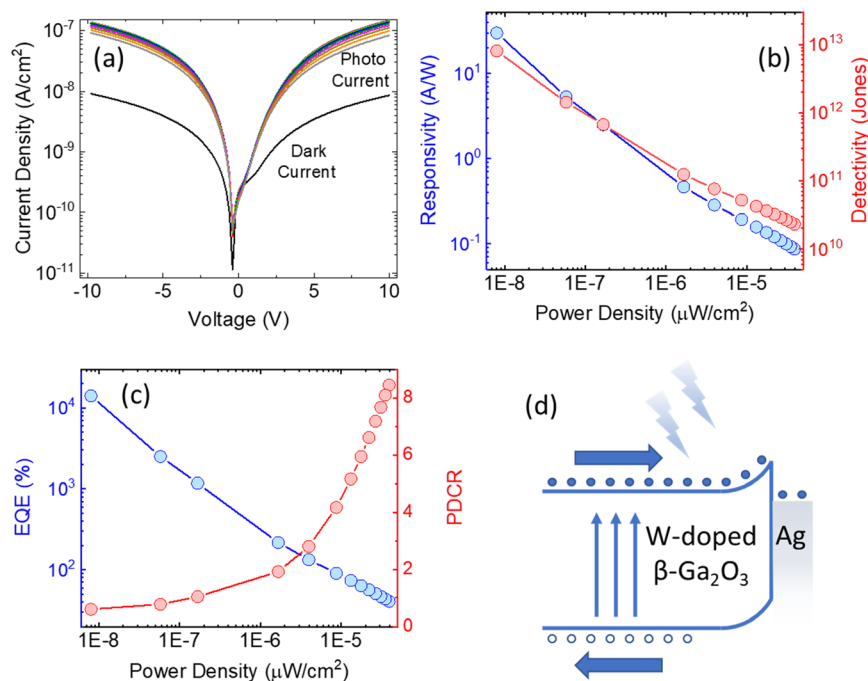$$\text{EQE} = \frac{R_\lambda hc}{e\lambda} \times 100\% \tag{9}$$

Fig. 10 Steady-state response: (a) dark and photocurrent under forward/reverse bias; (b) incident power-dependent responsivity and detectivity at 265 nm irradiation and 10 V forward bias; (c) incident power-dependent EQE and PDCR at 265 nm irradiation and 10 V forward bias; (d) empirical band diagram at the interface of the metal–semiconductor junction.

$$\text{PDCR} = \frac{j_{p,\lambda} - j_d}{j_d} \tag{10}$$

The terms photocurrent density, dark-current density, incident photon power density, charge of an electron, and wavelength are denoted as j_p, j_d, P, e, and λ, correspondingly. The data shown in Fig. 10(b and c) illustrate the R, D^*, EQE, and PDCR of 100 mTorr sample at 10 V forward bias under varying UV (265 nm) illumination power density. The aforementioned comparison shows 100 mTorr sample shows the best photodetection performance with 30 A/W R, 8×10^{12} D^*, 1.4×10^4 EQE, and 8.4 PDCR, respectively.

4. Conclusions

Nanocrystalline Ga–W–O films were fabricated by PLD varying the oxygen partial pressure in wide range (5–200 mTorr). The effect of varying pO_2 on the structure, surface chemistry, and optical characteristics of the resultant Ga–W–O films was examined by performing comprehensive characterization. The W-incorporated Ga_2O_3 films did not show any secondary phase development. The structural and chemical studies indicate that the chemistry of W varies with pO_2 and significantly affects the overall chemical and optical properties of Ga–W–O films. At lower working pressures, W^{5+} formation is more common when adatom mobility is strong; at higher working pressures, W^{6+} formation is more favorable due to decreased migration energy. On the other hand, when pO_2 increases, the GWO films' valence band maxima shift to higher energies, indicating that O 2p states predominate on the valence band. The optical band gap does not exhibit significant variation; rather, the luminescence peak exhibits a tiny blue shift, which points the way for a selective incorporation of W into the Ga_2O_3 matrix. The results illustrate that meticulous manipulation of the deposition parameters enables the adjustment of the morphology, microstructure and optical characteristics of the GWO films. The structure–property correlation established in this study can potentially be valuable in producing W-doped β-Ga_2O_3 films with excellent structural and optical properties, which might be utilized in optoelectronic and photonic applications.

Data availability

All authors certify that they have participated sufficiently in the research work presented in this manuscript and take responsibility for the content, including participation in the concept, design, analysis, writing, or revision of the manuscript. The data that support the claims and conclusions of the manuscript are deposited into the manuscript already. The other data may be available from the corresponding author upon reasonable request.

Conflicts of interest

There are no conflicts to declare.

© 2024 The Author(s). Published by the Royal Society of Chemistry

RSC Appl. Interfaces, 2024, **1**, 1395–1409 | **1407**

Acknowledgements

References

1 J. E. N. Swallow, C. Vorwerk, P. Mazzolini, P. Vogt, O. Bierwagen, A. Karg, M. Eickhoff, J. Schörmann, M. R. Wagner, J. W. Roberts, P. R. Chalker, M. J. Smiles, P. Murgatroyd, S. A. Razek, Z. W. Lebens-Higgins, L. F. J. Piper, L. A. H. Jones, P. K. Thakur, T.-L. Lee, J. B. Varley, J. Furthmüller, C. Draxl, T. D. Veal and A. Regoutz, *Chem. Mater.*, 2020, **32**, 8460–8470.

2 I. Cora, F. Mezzadri, F. Boschi, M. Bosi, M. Čaplovičová, G. Calestani, I. Dódony, B. Pécz and R. Fornari, *CrystEngComm*, 2017, **19**, 1509–1516.

3 D. Das, F. Sanchez, D. J. Barton, S. Tan, V. Shutthanandan, A. Devaraj and C. V. Ramana, *Adv. Mater. Technol.*, 2023, **8**, 2300014.

4 K. D. Leedy, K. D. Chabak, V. Vasilyev, D. C. Look, J. J. Boeckl, J. L. Brown, S. E. Tetlak, A. J. Green, N. A. Moser, A. Crespo, D. B. Thomson, R. C. Fitch, J. P. McCandless and G. H. Jessen, *Appl. Phys. Lett.*, 2017, **111**, 012103.

5 D. Guo, Y. Su, H. Shi, P. Li, N. Zhao, J. Ye, S. Wang, A. Liu, Z. Chen, C. Li and W. Tang, *ACS Nano*, 2018, **12**, 12827–12835.

6 S.-H. Yuan, S.-L. Ou, S.-Y. Huang and D.-S. Wuu, *ACS Appl. Mater. Interfaces*, 2019, **11**, 17563–17569.

7 Y. Huang, K. Saito, T. Tanaka and Q. Guo, *Appl. Phys. Lett.*, 2021, **119**, 062107.

8 Q. Guo, K. Saito and T. Tanaka, *ACS Appl. Electron. Mater.*, 2023, **5**, 4002–4013.

9 C. Joishi, Z. Xia, J. McGlone, Y. Zhang, A. R. Arehart, S. Ringel, S. Lodha and S. Rajan, *Appl. Phys. Lett.*, 2018, **113**, 123501.

10 G. Gutierrez, E. M. Sundin, P. G. Nalam, V. Zade, R. Romero, A. N. Nair, S. Sreenivasan, D. Das, C. Li and C. V. Ramana, *J. Phys. Chem. C*, 2021, **125**, 20468–20481.

11 D. Das, F. S. Escobar, P. G. Nalam, P. Bhattacharya and C. Ramana, *J. Lumin.*, 2022, **248**, 118960.

12 E. G. Víllora, K. Shimamura, Y. Yoshikawa, T. Ujiie and K. Aoki, *Appl. Phys. Lett.*, 2008, **92**, 202120.

13 Y. Wang, J. Su, Z. Lin, J. Zhang, J. Chang and Y. Hao, *J. Mater. Chem. C*, 2022, **10**, 13395–13436.

14 E. V. Favela, H. M. Jeon, K. D. Leedy, K. Zhang, S.-W. Tung, F. S. Escobar, C. V. Ramana and L. M. Porter, *J. Vac. Sci. Technol., B: Nanotechnol. Microelectron.: Mater., Process., Meas., Phenom.*, 2023, **41**, 032205.

15 R. Sun, Y. K. Ooi, P. T. Dickens, K. G. Lynn and M. A. Scarpulla, *Appl. Phys. Lett.*, 2020, **117**, 052101.

16 V. Vasyltsiv, A. Luchechko, Y. Zhydachevskyy, L. Kostyk, R. Lys, D. Slobodzyan, R. Jakieła, B. Pavlyk and A. Suchocki, *J. Vac. Sci. Technol., A*, 2021, **39**, 033201.

17 R. Chen, D. Wang, J. Liu, B. Feng, H. Zhu, X. Han, C. Luan, J. Ma and H. Xiao, *Cryst. Growth Des.*, 2022, **22**, 5285–5292.

18 V. Zade, B. Mallesham, S. Roy, V. Shutthanandan and C. V. Ramana, *ECS J. Solid State Sci. Technol.*, 2019, **8**, Q3111–Q3115.

19 E. J. Rubio and C. V. Ramana, *Appl. Phys. Lett.*, 2013, **102**, 191913.

20 A. A. Dakhel, *Microelectron. Reliab.*, 2012, **52**, 1050–1054.

21 M. Xian, C. Fares, F. Ren, B. P. Gila, Y.-T. Chen, Y.-T. Liao, M. Tadjer and S. J. Pearton, *J. Vac. Sci. Technol., B: Nanotechnol. Microelectron.: Mater., Process., Meas., Phenom.*, 2019, **37**, 061201.

22 Y. Yao, R. Gangireddy, J. Kim, K. K. Das, R. F. Davis and L. M. Porter, *J. Vac. Sci. Technol., B: Nanotechnol. Microelectron.: Mater., Process., Meas., Phenom.*, 2017, **35**, 03D113.

23 Y. Yao, D. Sang, L. Zou, Q. Wang and C. Liu, *Nanomaterials*, 2021, **11**, 2136.

24 S. Cong, F. Geng and Z. Zhao, *Adv. Mater.*, 2016, **28**, 10518–10528.

25 H. Zheng, J. Z. Ou, M. S. Strano, R. B. Kaner, A. Mitchell and K. Kalantar-zadeh, *Adv. Funct. Mater.*, 2011, **21**, 2175–2196.

26 F. Mehmood, R. Pachter, N. R. Murphy, W. E. Johnson and C. V. Ramana, *J. Appl. Phys.*, 2016, **120**, 233105.

27 N. Makeswaran, D. Das, V. Zade, P. Gaurav, V. Shutthanandan, S. Tan and C. Ramana, *ACS Appl. Nano Mater.*, 2021, **4**, 3331–3338.

28 C. V. Ramana, D. Das, G. Gutierrez, F. S. Manciu and V. Shutthanandan, *J. Mater. Sci.*, 2022, **57**, 11170–11188.

29 M. Bandi, V. Zade, S. Roy, A. N. Nair, S. Seacat, S. Sreenivasan, V. Shutthanandan, C. G. Van de Walle, H. Peelaers and C. V. Ramana, *Cryst. Growth Des.*, 2020, **20**, 1422–1433.

30 B. Mallesham, S. Roy, S. Bose, A. N. Nair, S. Sreenivasan, V. Shutthanandan and C. V. Ramana, *ACS Omega*, 2020, **5**, 104–112.

31 D. Das, G. Gutierrez and C. V. Ramana, *ACS Omega*, 2023, **8**, 11709–11716.

32 N. Fairley, A. Carrick and N. Fairly, *The casa cookbook*, Acolyte science Cheshire, 2005.

33 M. C. Biesinger, *Appl. Surf. Sci.*, 2022, **597**, 153681.

34 P. G. Nalam, D. Das, V. Shutthanandan and C. V. Ramana, *ACS Appl. Opt. Mater.*, 2023, **1**, 1761–1776.

35 M. H. Engelhard, D. R. Baer, A. Herrera-Gomez and P. M. A. Sherwood, *J. Vac. Sci. Technol., A*, 2020, **38**, 063203.

36 P. M. A. Sherwood, *Surf. Interface Anal.*, 2019, **51**, 589–610.

37 Q. A. Drmosh, N. A. Al-Muhaish, Y. A. Al Wajih, M. W. Alam and Z. H. Yamani, *Chem. Phys. Lett.*, 2021, **776**, 138659.

38 Y. Liu, N. Jiang, Y. Liu, D. Cui, C.-F. Yu, H. Liu and Z. Li, *Ceram. Int.*, 2021, **47**, 22416–22423.

39 G. H. Major, V. Fernandez, N. Fairley, E. F. Smith and M. R. Linford, *J. Vac. Sci. Technol., A*, 2022, **40**, 063201.

40 N. Makeswaran, C. Orozco, A. K. Battu, E. Deemer and C. V. Ramana, *Materials*, 2022, **15**, 754.

41 A. Ojeda-G-P, M. Döbeli and T. Lippert, *Adv. Mater. Interfaces*, 2018, **5**, 1701062.

42 N. A. Shepelin, Z. P. Tehrani, N. Ohannessian, C. W. Schneider, D. Pergolesi and T. Lippert, *Chem. Soc. Rev.*, 2023, **52**, 2294–2321.

43 D. C. Ghosh and R. Biswas, *Int. J. Mol. Sci.*, 2003, **4**, 379–407.

44 R. D. Shannon, *Acta Crystallogr., Sect. A: Cryst. Phys., Diffr., Theor. Gen. Crystallogr.*, 1976, **32**, 751–767.

45 H. Kalhori, M. Ranjbar, H. Farrokhpour and H. Salamati, *J. Laser Appl.*, 2019, **31**, 032018.

46 D. I. Miakota, R. R. Unocic, F. Bertoldo, G. Ghimire, S. Engberg, D. Geohegan, K. S. Thygesen and S. Canulescu, *Nanoscale*, 2022, **14**, 9485–9497.

47 K. J. Lethy, D. Beena, R. Vinod Kumar, V. P. Mahadevan Pillai, V. Ganesan, V. Sathe and D. M. Phase, *Appl. Phys. A: Mater. Sci. Process.*, 2008, **91**, 637–649.

48 O. M. Hussain, A. S. Swapnasmitha, J. John and R. Pinto, *Appl. Phys. A: Mater. Sci. Process.*, 2005, **81**, 1291–1297.

49 R. V. Chintalapalle, S. Utsunomiya, C. M. Julien and U. Becker, *ECS Trans.*, 2006, **1**, 37–42.

50 J. B. Varley, J. R. Weber, A. Janotti and C. G. Van de Walle, *Appl. Phys. Lett.*, 2010, **97**, 142106.

51 L. Dong, R. Jia, B. Xin, B. Peng and Y. Zhang, *Sci. Rep.*, 2017, **7**, 40160.

52 Y. S. Zou, Y. C. Zhang, D. Lou, H. P. Wang, L. Gu, Y. H. Dong, K. Dou, X. F. Song and H. B. Zeng, *J. Alloys Compd.*, 2014, **583**, 465–470.

53 H. S. Han, W. Park, S. W. Hwang, H. Kim, Y. Sim, S. Surendran, U. Sim and I. S. Cho, *J. Catal.*, 2020, **389**, 328–336.

54 M. Mai, X. Ma, H. Zhou, M. Ye, T. Li, S. Ke, P. Lin and X. Zeng, *J. Alloys Compd.*, 2017, **722**, 913–919.

55 H. Kalhori, S. B. Porter, A. S. Esmaeily, M. Coey, M. Ranjbar and H. Salamati, *Appl. Surf. Sci.*, 2016, **390**, 43–49.

56 M. Jaquez, K. M. Yu, M. Ting, M. Hettick, J. F. Sánchez-Royo, M. Wełna, A. Javey, O. D. Dubon and W. Walukiewicz, *J. Appl. Phys.*, 2015, **118**, 215702.

57 A. F. M. A. U. Bhuiyan, Z. Feng, J. M. Johnson, H.-L. Huang, J. Hwang and H. Zhao, *Appl. Phys. Lett.*, 2020, **117**, 252105.

58 H. Peelaers, J. B. Varley, J. S. Speck and C. G. Van de Walle, *Appl. Phys. Lett.*, 2018, **112**, 242101.

59 T. S. Wang, W. Li, C. Y. Ni and A. Janotti, *Phys. Rev. Appl.*, 2018, **10**, 011003.

60 J. E. N. Swallow, R. G. Palgrave, P. A. E. Murgatroyd, A. Regoutz, M. Lorenz, A. Hassa, M. Grundmann, H. von Wenckstern, J. B. Varley and T. D. Veal, *ACS Appl. Mater. Interfaces*, 2021, **13**, 2807–2819.

61 S. Roy and C. V. Ramana, *J. Mater. Sci. Technol.*, 2021, **67**, 135–144.

62 R. Rao, A. M. Rao, B. Xu, J. Dong, S. Sharma and M. K. Sunkara, *J. Appl. Phys.*, 2005, **98**, 094312.

63 B. C. Keswani, R. S. Devan, R. C. Kambale, A. R. James, S. Manandhar, Y. D. Kolekar and C. V. Ramana, *J. Alloys Compd.*, 2017, **712**, 320–333.

64 V. S. Puli, D. K. Pradhan, S. Adireddy, R. Martínez, P. Silwal, J. F. Scott, C. V. Ramana, D. B. Chrisey and R. S. Katiyar, *J. Phys. D: Appl. Phys.*, 2015, **48**, 355502.

65 C. V. Ramana, B. S. Naidu, O. M. Hussain and R. Pinto, *J. Phys. D: Appl. Phys.*, 2001, **34**, L35.

66 O. M. Hussain, K. Srinivasa Rao, K. V. Madhuri, C. V. Ramana, B. S. Naidu, S. Pai, J. John and R. Pinto, *Appl. Phys. A: Mater. Sci. Process.*, 2002, **75**, 417–422.

67 B. Johnson, J. N. Hilfiker and M. R. Linford, *Vacuum Technology & Coating*, 2019, pp. 32–35.

68 D. I. Patel, D. Shah, J. N. Hilfiker and M. R. Linford, *Vac. Technol. Coat.*, 2019, **20**, 34–37.

69 J. Orava, T. Wágner, J. Šik, J. Přikryl, M. Frumar and L. Beneš, *J. Appl. Phys.*, 2008, **104**, 043523.

70 N. Nosidlak, P. Dulian, D. Mierzwiński and J. Jaglarz, *Coatings*, 2020, **10**, 980.

71 H. Kröncke, F. Maudet, S. Banerjee, J. Albert, S. Wiesner, V. Deshpande and C. Dubourdieu, *J. Vac. Sci. Technol., A*, 2021, **39**, 052408.

72 P. Makuła, M. Pacia and W. Macyk, *J. Phys. Chem. Lett.*, 2018, **9**, 6814–6817.

73 D. Das, N. Makeswaran, F. S. Escobar, S. Tan and C. V. Ramana, *Thin Solid Films*, 2022, **758**, 139425.

74 T. Onuma, Y. Nakata, K. Sasaki, T. Masui, T. Yamaguchi, T. Honda, A. Kuramata, S. Yamakoshi and M. Higashiwaki, *J. Appl. Phys.*, 2018, **124**, 075103.

75 S. Rafique, L. Han and H. Zhao, *Phys. Status Solidi A*, 2017, **214**, 1700063.

76 K. Arora, N. Kumar, P. Vashishtha, G. Gupta and M. Kumar, *J. Phys. D: Appl. Phys.*, 2021, **54**, 165102.

77 H. Peelaers and C. G. Van de Walle, *Phys. Rev. B*, 2016, **94**, 195203.

© 2024 The Author(s). Published by the Royal Society of Chemistry

RSC Appl. Interfaces, 2024, **1**, 1395–1409 | **1409**